Key Points:

- A satellite product ensemble was used to locate and quantify the hemispheric and seasonal contrast in cloud top thermodynamic phase
- At −30 °C, half of the liquid cloud tops observed in the southern hemisphere would glaciate in the northern hemisphere
- The new product ensemble is more reliable than the individual products and suggests a previous underestimation of the cloud-phase contrasts

Supporting Information:

- Supporting Information S1

Correspondence to:

D. Villanueva,
villanueva@tropos.de

Hemispheric and Seasonal Contrast in Cloud Thermodynamic Phase From A-Train Spaceborne Instruments

Diego Villanueva[1] [ID]**, Fabian Senf[1]** [ID]**, and Ina Tegen[1]** [ID]

[1]Modeling of Atmospheric Processes, Leibniz Institute for Tropospheric Research (TROPOS), Leipzig, Germany

Abstract Aerosol-cloud interactions are an important source of uncertainty in current climate models. To understand and quantify the influence of ice-nucleating particles in cloud glaciation, it is crucial to have a reliable estimation of the hemispheric and seasonal contrast in cloud top phase, which is believed to result from the higher dust aerosol loading in boreal spring. For this reason, we locate and quantify these contrasts by combining three different A-Train cloud-phase products for the period 2007–2010. These products rely on a spaceborne lidar, a lidar-radar synergy, and a radiometer-polarimeter synergy. We show that the cloud-phase from the product combination is more reliable and that the estimation of the hemispheric and seasonal contrast has a lower error compared to the individual products. To quantify the contrast in cloud-phase, we use the hemispheric difference in ice cloud frequency normalized by the liquid cloud frequency in the southern hemisphere between −42 °C and 0 °C. In the midlatitudes, from −15 to −30 °C, the hemispheric contrasts increase with decreasing temperature. At −30 °C, the hemispheric contrast varies from 29% to 39% for the individual cloud-phase products and from 52% to 73% for the product combination. Similarly, in the northern hemisphere, we assess the seasonal contrast between spring and fall normalized by the liquid cloud frequency during fall. At −30 °C, the seasonal contrast ranges from 21% to 39% for the individual cloud-phase products and from 54% to 75% for the product combination.

Plain Language Summary The influence of atmospheric particles on clouds is one of the main unknowns in climate predictions. Particularly, the cloud glaciation process and its dependence on desert dust and soot particles are not well-understood. To better understand the differences in cloud glaciation between hemispheres, we counted liquid and ice cloud tops, as observed from four different satellites, during 4 years. Combining these observations, we could confirm a higher frequency of ice cloud tops during spring in the northern hemisphere. We found that the contrast between hemispheres is higher than previously thought. These results will help to improve our understanding of cloud glaciation processes, which can be valuable for future climate predictions and for understanding the impact of aerosols on radiation and precipitation.

1. Introduction

Where do clouds glaciate? Ice clouds are more frequent in the northern hemisphere than in the southern hemisphere (Kanitz et al., 2011; Morrison et al., 2011; Tan et al., 2014). Understanding this contrast is of great importance for climate predictions, as liquid clouds reflect more shortwave radiation compared to ice clouds (Bodas-Salcedo et al., 2014; Matus & L'Ecuyer, 2017; Trenberth & Fasullo, 2010; Vergara-Temprado et al., 2018). Specifically, in the southern hemisphere, climate models show that the frequency of liquid clouds is associated with changes in sea surface temperature and the atmospheric cross-equatorial energy transport (Hawcroft et al., 2017). Moreover, there is high variability in the cloud-phase partitioning between climate models, which has been associated with uncertainties in cloud fraction and climate sensitivity (McCoy et al., 2016; Tan et al., 2016; Zelinka et al., 2020).

Previous studies have tried to elucidate the hemispheric and seasonal differences in cloud-phase by using spaceborne retrievals of aerosol loading and cloud-phase from lidar and radar retrievals. Several studies have attributed the north-south contrast in cloud-phase to the hemispheric differences in the concentration of ice-nucleating particles (INP) such as dust aerosol (Bruno et al., 2021; Choi et al., 2010; Kawamoto
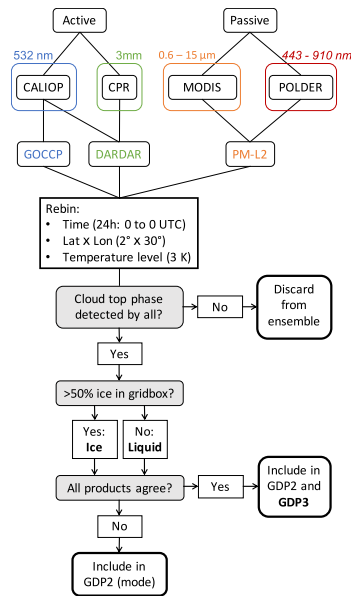
Figure 1. Diagram showing the different cloud-phase products used to derive the GDP ensemble (GOCCP-DARDAR-PML2). The colored boxes correspond to the spaceborne instruments used for each product (colored acronyms) and the colored values represent the wavelength used for the classification. In case of multiband instruments, the wavelength range is shown. Values in italics denote multiangle observations of total and polarized radiance. The lower part of the diagrams shows how the products are rebinned and processed to create the GDP2 and GDP3 ensembles.

et al., 2020; Tan et al., 2014; Vergara-Temprado et al., 2017; Zhang et al., 2018). Due to land-ocean distribution, the largest dust sources (such as the Saharan Desert) are located in the northern hemisphere. Additionally, during spring in the northern hemisphere, dust concentrations are generally higher than in fall (Cowie et al., 2014; Luo et al., 2015). In the same season, it has been shown that clouds tend to produce more ice (Zhang et al., 2018). However, this seasonal contrast has received less attention so far.

In general, the spatiotemporal correlation between mineral dust and ice cloud frequency suggests that dust INP may be controlling the north-south contrast in cloud-phase (Seifert et al., 2010; Tan et al., 2014; Villanueva et al., 2020; Zhang et al., 2012). However, dust concentrations are also correlated with other meteorological factors like humidity, thermal stability, and vertical velocity, which are in turn correlated to the ice cloud frequency (Li et al., 2017; Sullivan et al., 2016). This has led to a debate over whether dust INP or meteorology dominates the observed variability of cloud glaciation. Therefore, assessing the hemispheric and seasonal cloud-phase contrast in detail may lead to a better understanding of dust-driven cloud glaciation.

Most satellite cloud-phase products available are based on passive radiometers (e.g., sorted as Satellite-Instrument-Product: NOAA-AVHHR-PATMOS, Terra-MODIS-C6, and METEOSAT-SEVIRI-CLAAS). Active instruments capable of retrieving cloud-phase, like lidar and radar, are more scarce. From 2007 to 2010, several instruments capable of retrieving cloud-phase were synchronized to follow the same orbit ("A-Train"). During this period, a radiometer, lidar, radar, and a multiangle radiometer retrieved cloud properties almost without interruption. Each of these instruments has been used individually to assess cloud-phase globally based on different cloud physical features (Hu et al., 2009; Huang et al., 2012; Riedi et al., 2010). Moreover, synergies between them have been proven to be even more successful than the individual products (Delanoë & Hogan, 2010; Ewald et al., 2021; Riedi et al., 2010). As extension to Villanueva et al. (2020), where only the CALIOP-GOCCP product was used to assess the temporal (daily) variability of cloud-phase, this study combines the different products available from the A-Train to locate and quantify the seasonal and hemispheric contrast of cloud top phase. Such a combined quantification has been lacking up to now. These contrasts in cloud top phase can then be compared to the variability of dust aerosol to assess the potential role of dust INP. Furthermore, we expect that this new information may serve as a benchmark for improving dust-driven cloud glaciation in climate simulations.

2. Data and Methods

2.1. A-Train Cloud-Phase Products

Figure 1 shows the spaceborne instruments and products from the A-Train used in this study for the period 2007–2010 and the respective flow diagram of how we generate the GDP ensembles (GOCCP-DAR-DAR-PML2). The Cloud-Aerosol LIdar with Orthogonal Polarization (CALIOP) onboard CALIPSO (Wu et al., 2014) and the Cloud Profiling Radar (CPR) on board CloudSat are both active instruments. In the GCM-Oriented Cloud Calipso Product (CALIPSO-GOCCP v3.0; Cesana & Chepfer, 2013), the lidar depolarization measured by CALIOP is compared against an empirical threshold to retrieve the cloud-phase, where higher depolarization ratios are associated with ice crystals. In the liDAR-raDAR (DARDAR-MASK v2.0) product (Ceccaldi et al., 2013; Delanoë & Hogan, 2010), a decision tree is used to retrieve the cloud-phase, where the main criterion is the cloud detection by the radar reflectivity (Mioche et al., 2014). A higher radar reflectivity is associated with larger particles such as ice crystals. In both the DARDAR and the GOCCP product, the detection of the cloud top is based on the CALIOP attenuated backscattering ratio. The cloud top temperature is then derived from the ECMWF-AUX reanalysis for the DARDAR product and from the
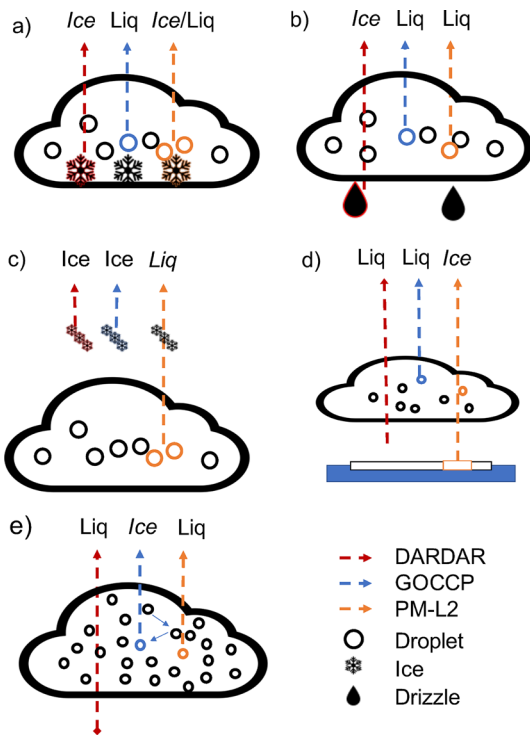
Figure 2. Diagram showing the known retrieval biases associated to different cloud types for the different products. (a) Ice virgae in mixed-phase clouds. (b) Drizzle from liquid clouds. (c) Cirrus over liquid clouds. (d) Thin clouds and surface albedo. (e) Multiscattering effects. Retrievals in italics represent errors.

GEOS-GMAO reanalysis for the GOCCP product. To avoid artifacts in the lidar due to daylight scattering, only nighttime values are included for the GOCCP product. On the other hand, both daytime and nighttime retrievals are included for the DARDAR product.

The MODIS (MODerate resolution Imaging Spectroradiometer) onboard the Aqua satellite and the POLDER-3 (Polarization and Directionality of the Earth Reflectance) onboard the PARASOL satellite are both passive instruments. Different algorithms can be used with different radiometers to retrieve cloud top phase (Pavolonis et al., 2005; Riedi et al., 2010, for the AVHHR and MODIS instrument, respectively). The MODIS Short-Wave-InfraRed (SWIR) product uses the ratio between the measured reflectance in the near-infrared and in the visible spectra to retrieve the cloud-phase, where low ratios are associated with ice crystals. The MODIS Thermal-InfraRed (TIR) product uses the Brightness Temperature Difference (BTD) between the 8.5-μm and 11-μm bands. This difference, also known as BTD[8.5–11], is used to retrieve the cloud-phase, where high positive values are associated with ice crystals. The POLDER-3 instrument can retrieve the polarized and total radiance. Therefore, it can estimate the polarization ratio for different scattering angles. Thus, in the POLAR algorithm, a decreasing polarization with increasing scattering angle is associated with ice crystals. Additionally, a peak in the polarization near 140° (rainbow effect) implies the presence of cloud droplets (Riedi et al., 2010).

The PARASOL and Aqua/MODIS combination (PM-L2) product weights the MODIS-SWIR, MODIS-TIR, and POLDER-3-POLAR products to make a final decision about the cloud-phase at cloud top. For each decision, a confidence level is calculated depending on which products agree on the same cloud-phase. A confidence flag of 0 means that all three products (SWIR, TIR, and POLAR) agree with high confidence on the ice-phase and a flag of 200 means that all agree on the liquid-phase. To distinguish between the liquid-phase and ice-phase, we use only confidences below 25 or above 175. We chose this threshold to optimize the agreement with the active products, focusing on the range of the observed frequency of ice cloud tops. With the 25/175 confidence threshold, the cloud ice frequency ranges from 0.05 to 0.95. Using a 10/190 confidence threshold resulted in an ice frequency range from 0.02 to 0.99 but only 60% of the sample size relative to the 25/175 threshold. In contrast, a 50/150 confidence threshold resulted in an ice frequency range from 0.12 to 0.86 with 150% the sample size relative to the 25/175 threshold. Additionally, Coopman et al. (2020) showed that high confidence thresholds (20/180) result in a higher spatial correlation between cloud droplet size and cloud-phase. Finally, because the PM-L2 product relies on passive instruments, only daytime retrievals are included.

It is very challenging to determine why the cloud products may retrieve a different cloud top phase in a given cloud scenario. However, some known issues have already been discussed in detail in the literature (Huang et al., 2012, 2015; Riedi et al., 2010).

The most important factors that lead to different decisions are the size of cloud droplets and ice particles, the Cloud Optical Thickness (COT), and underlying clouds or surface. Figure 2 shows some known microphysical settings that may lead to a wrong cloud top phase retrieval by some of the cloud products. When the number or size of ice particles at cloud top is high enough, the DARDAR algorithm will classify the top as ice regardless of the number of cloud droplets present (see Figure 2a). Similarly, drizzle droplets can be large enough to be mistakenly classified as ice (Zhang et al., 2018), especially at temperatures above −10 °C (see Figure 2b). The POLAR algorithm applied to POLDER-3 is strongly sensitive to the cloud optical thickness. For cirrus clouds overlying a liquid cloud, simulations showed that the POLAR algorithm will only retrieve the ice-phase if the cloud optical thickness is higher than 2 (see Figure 2c; Riedi et al., 2010). On the other hand, in the TIR and SWIR algorithm applied to MODIS and included in PM-L2, the retrieved

emissivity and reflectance may be dominated by the clouds or surface under the cloud, especially for thin clouds (see Figure 2d; Riedi et al., 2010). In the GOCCP product, if many small cloud droplets are present, multiscattering effects may result in a high depolarization ratio, even when no ice is present (Hu et al., 2009, see Figure 2e). The spatial-angular (3D) characteristics of clouds may also influence the retrieved reflectance and radiance from the MODIS and POLDER instruments. For example, the polarization signal from POLDER becomes weak and ambiguous for broken clouds (Riedi et al., 2010).

We obtain the dust aerosol loading from the Copernicus Atmosphere Monitoring Service (CAMS) reanalysis (Inness et al., 2019). In the CAMS reanalysis, dust emission is a function of the wind near the surface (10 m), vegetation, soil moisture, and surface albedo. The simulated dust mixing ratio is corrected by assimilating the aerosol optical thickness at 550 nm retrieved by MODIS. Dust is removed in the model by dry and wet deposition.

2.2. Collocation and GDP2 Ensemble

Similar to the three-member combination of cloud-phase products in the PM-L2 product, we combine the GOCCP, DARDAR, and PM-L2 products to create a daily cloud top phase ensemble.

Temporal merging: For each day, we merge both the ascending and descending overpasses temporally from 0 to 24 UTC (For GOCCP only nighttime retrievals).

Vertical collocation: For the active products, only the top cloudy pixels from each instant vertical profile were included. Using the cloud top temperature available from each product, we assign each pixel to a 3 K temperature bin between −42 and 3 °C. We note that the cloud top temperature is derived differently for each product. The GOCCP and DARDAR products include an interpolation of atmospheric reanalyzes, from which we use the temperature corresponding to the height of the top cloudy pixel. For the PM-L2 product, the cloud top temperature retrieved from MODIS is used instead. Other than for the active retrievals, the depth of the cloud top retrievals from MODIS and POLDER depends on the optical thickness of the cloud and may result in a bias in cloud top phase for thin clouds (Stengel et al., 2020). However, a sensitivity study showed that the difference in the ice cloud top frequency between thin (COT < 2) and thick (COT > 2) clouds was low (less than ±1%).

Horizontal collocation: We regrid all three products to a 2° × 30°(lat × lon) grid by averaging the binary cloud-phase flags contained inside each gridbox. Therefore, for the active products, each gridbox is sampled only through the narrow swath(s) crossing it. We refer to this average as the daily frequency phase ratio (FPR_{daily}), the ratio of ice pixels to the total (liquid + ice) cloudy pixels included in each gridbox. The 2° × 30° grid was chosen to optimize the overlap between the active instruments (narrow swaths) and passive instruments (wide swaths). For a visualization of the collocation method, please refer to the supporting information.

For each product, we use the frequency of ice pixels to classify each volume gridbox as either liquid or ice. After the collocation described above, for each product we obtain a 3-dimensional FPR_{daily} on a 3 K × 2° × 30° space (temperature × lat × lon). This FPR_{daily} represents the frequency of ice pixels within each gridbox at each temperature bin. Most of the regridded FPR_{daily} values for the different products lay below 0.1 or above 0.9; namely 75%, 71%, and 81% of the total sample size for the GOCCP, DARDAR, and PM-L2 products, respectively. Therefore, to simplify the combination of products, we rounded the FPR_{daily} of each individual product to the nearest integer (0 for liquid and 1 for ice). As a result, FPR_{daily} follows a binary distribution.

We combine the cloud-phase products by finding the cloud-phase for which most of the products agree. To produce the ensemble of cloud-phase products (see Figure 1), we discard the time steps where one or more products are missing. Because at least two products will always agree (on either liquid or ice), the cloud-phase is set to the mode between the three products. We refer to this three-member ensemble as the GDP2 ensemble (because at least two products agree).

The FPR_{daily} in the GDP2 ensemble corresponds to a daily phase classification dominated by the cloud top phase of stratiform clouds, which can be aggregated over time to derive a frequency of ice clouds. In the product ensemble, FPR_{daily} will be flagged as "missing" for the time steps where the cloud-phase products do not overlap. Therefore, the averaging order will play a role in the results. To avoid a bias toward the
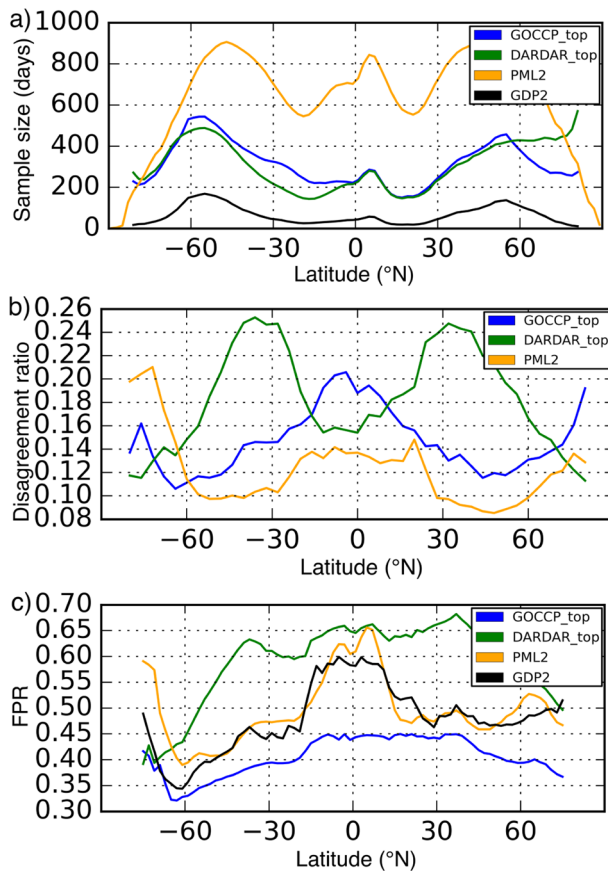
Figure 3. Zonal-vertical mean of (a) gridbox sample size in days (b) disagreement ratio for the individual cloud-phase products relative to the GDP2 ensemble (c) frequency of ice cloud tops for the different cloud-phase products. Averaged between 0 and −42 °C.

levels and gridboxes containing more data, we average in the following order: time, longitude, latitude, and temperature. After aggregating the FPR_{daily} within a certain time frequency (monthly in this work), it can be interpreted as the ice cloud top frequency ($FPR_{monthly}$ or FPR for short) The FPR_{daily} is defined within a 2° × 30° gridbox, so that the the aggregated FPR will be dominated by the thermodynamic phase of horizontally broad clouds (i.e., stratiform clouds). The distinction between the binary frequency FPR_{daily} and the monthly aggregated frequency FPR is important for the uncertainty analysis, because FPR_{daily} follows a binary distribution, while FPR follows a normal distribution for high sample sizes.

2.3. Sample Size

After the regridding described above, FPR_{daily} follows a binomial distribution. In this distribution, the probability of finding an ice cloud top will be p $(0 − 1)$, which depends mainly on temperature. Therefore, after aggregating (averaging) n measurements of cloud-phase (FPR_{daily}), the standard deviation of the instant ("observed") frequency FPR around the expected ("real") frequency p can be estimated as:

$$\sigma_{FPR} = \sqrt{\frac{p(1-p)}{n}}. \tag{1}$$

In other words, the sample size will have an impact on the uncertainty in FPR. In addition, the spatiotemporal variability of cloud-phase (e.g., regional differences and seasonal cycle) and retrievals errors will also introduce an intermonthly spread in the expected frequency p, contributing to the total spread σ_{FPR}.

For the period 2007–2010, a total of 1,200 days had at least one retrieval for each cloud-phase product. In other words, for the average gridbox (2° × 30°), the timelines of the individual instruments overlap for 82% of the period. During this period, for the ensemble and the individual products, the sample size is distributed relatively homogenously between −42 and +3 °C. However, between −10 and −30 °C the sample size decreases by about 25% for the GDP2 ensemble and the DARDAR product (see supporting information). Figure 3 shows the zonal-vertical mean of the sample size, disagreement ratio, and frequency of ice cloud tops for the different phase products. Across latitudes, the sample size is similar in both hemispheres, especially between 75°N/S. The largest sample size is found near 55°N/S and at around 5°N (Figure 3a). These peaks coincide with the average position of the storm tracks and the intertropical convergence zone, respectively. The sample size of GOCCP product tends to be higher than in the DARDAR product because GOCCP is not limited by the availability of retrievals from the CPR instrument. However, we only include nighttime retrievals for GOCCP, and therefore the sample size decreases relative to DARDAR above 60°N, especially in summer.

The sample size of the GOCCP and DARDAR products is limited by the narrow swath of CALIOP. In contrast, the broader swath of the POLDER-3 instrument results in a sample size nearly twice as large as for the active products. However, for the GDP2 ensemble, the sample size drops to about a half compared to GOCCP and DARDAR. The sample size of GDP2 depends only on the spatiotemporal collocation between the individual gridded products. Therefore, to understand how each of these products affects the ensemble, we must first consider the two-member ensembles (DP: DARDAR and PM-L2; GP: GOCCP and PM-L2; GD: GOCCP and DARDAR). These ensembles are defined only when both members agree on the cloud-phase at cloud top. We define the collocation ratio as the sample size of the two-member ensemble divided by the maximal achievable sample size (assuming a perfect collocation). The collocation ratios are 69%, 66%, and 33% for the DP, GP, and GD ensembles, respectively. These collocation ratios show that the sample size of GDP2 is strongly limited by the poor collocation between the GOCCP and DARDAR products. We attribute

this poor collocation to a cloud top temperature underestimation (of −5 K in average) in the DARDAR product (derived from the ECMWF-AUX reanalysis) relative to the GOCCP product (GEOS-GMAO reanalysis) and to the MODIS retrievals. Additionally, due to the temporal collocation between the products, the GDP ensembles only include scenarios where clouds are detected in the same gridbox during nighttime (by DARDAR and/or GOCCP) and daytime (by DARDAR and/or PM-L2), which also contributes to the low collocation ratio for the GDP ensembles, as clouds need to be detected during two different satellite passes (during day and night).

3. Results

3.1. Agreement

To assess the single products with respect to the GDP2 ensemble, we define the disagreement ratio as the frequency of time steps where the cloud-phase from a given product is different to that from the ensemble. On average, the GDP2 ensemble disagrees with the GOCCP, DARDAR, and PM-L2 products 12%, 18%, and 10% of the time, respectively. Because we truncate the cloud-phase in the ensemble to a binary variable (liquid or ice), the GDP2 ensemble (the mode among the products) can either agree with all three products or disagree with at most one (see supporting information). Adding up the disagreement ratio for each product, we find that the GDP2 ensemble disagrees with one of the three products 40% of the time and, therefore, all three products agree 60% of the time. However, the disagreement ratio is not evenly distributed across different temperatures. For the single products, the maximum disagreement ratio occurs at the average glaciation temperature (for which the *FPR* equals 0.5) and drops to zero toward higher and lower temperatures, closely resembling a "bell" curve (see supporting information).

The highest disagreement is found at −22 °C, where the GDP2 ensemble disagrees with the GOCCP, DARDAR, and PM-L2 products 26%, 21%, and 24% of the time, respectively. Therefore, the ensemble disagrees with one of the products 71% of the time. In other words, at −22 °C, we would be almost as lucky trying to find an agreement between three coin tosses (disagreement of 75%) than between the three cloud top phase retrievals. At first, this may suggest that there is no safe way to tell which of the products is making the right decision. However, when independent products agree with each other (in our case, two of them always do), it is because different physical features are consistent with a certain phase. Therefore, it is reasonable to assume that the GDP2 ensemble is more reliable than the individual products. In fact, on average, no single pair of products agrees entirely (the lowest disagreement is 12% + 10% = 22% of the time between GOCCP and PM-L2), which reflects that the products are independent. Therefore, even when one of the products disagrees, the other two still provide a strong criterium to decide the cloud-phase. However, even if all three products always agree, there could be a bias shared by all products. Similarly, if one product always disagrees, it may still be more accurate than the other two.

The disagreement ratio of the single products is similar for both hemispheres (Figure 3b). However, the disagreement ratio of the GOCCP and PM-L2 products is lower in the midlatitudes than in the subtropics and high-latitudes, while the opposite occurs for the DARDAR product. As a result, in the midlatitudes, the DARDAR product disagrees roughly twice as frequently with the GDP2 ensemble compared to the GOCCP and PM-L2 products. The PM-L2 product shows the lowest disagreement ratio with the GDP2 product (in the midlatitudes and subtropics), the lowest bias (relative to GDP2), and the largest sample size. This suggests that, from all three cloud-phase products the PM-L2 product seems to be the most reliable.

3.2. Frequency Phase Ratio

The spaceborne lidar may fail to detect large ice particles, while the radar may detect a cloud even with very few ice particles. Therefore, the GOCCP product has the lowest *FPR* at all altitudes (except for Antarctica), while the DARDAR product has the highest *FPR* (Figure 3c). The *FPR* from the PM-L2 product lays mostly between the other two products and agrees better with the GDP2 ensemble, arguably because the PM-L2 also relies on multiple physical features at cloud top to retrieve the cloud-phase.

All three products and the GDP2 ensemble have a higher *FPR* near the subtropics. For the GOCCP product, the *FPR* increases toward the equator by about +0.10 starting from 60°S and 70°N. For DARDAR, the *FPR*
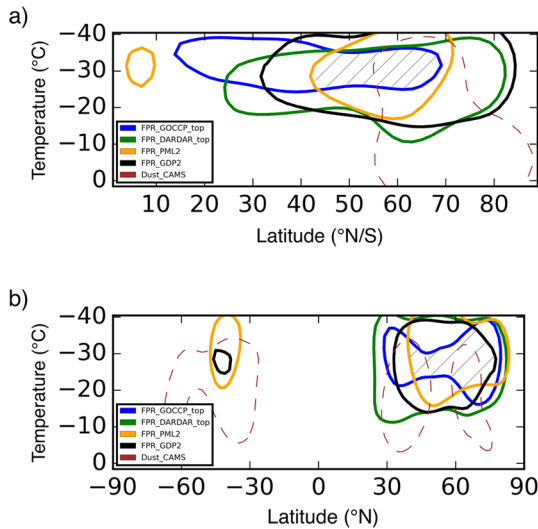
a)

b)

Figure 4. Contour plot enclosing the regions in the temperature-latitude space where (a) the normalized north-south difference in *FPR* at cloud top (Equation 2) is higher than +0.2 and (b) the normalized seasonal difference in *FPR* between MAM(SON) and SON(MAM) in the northern(southern) hemisphere is higher than +0.1. The hatched region corresponds to the zone where all products have a north-south(seasonal) contrast higher than +0.2(+0.1). The dashed contour encloses the regions where the dust loading is (a) 50 times higher in the northern hemisphere (b) three times higher during spring. A Gaussian filter was applied to smoothen the contours. FPR, frequency phase ratio; MAM, March-April-May; SON, September-October-November.

increases toward the subtropics (up to 40°S and 40°N) by about +0.20 starting at 70°S and 70°N, respectively. Finally, for PM-L2, the *FPR* increases by about +0.15 toward the equator but starting from 15°S and 15°N. As the sample size decreases toward Antarctica, fewer samples are available at the highest isotherms, which become underrepresented. Therefore, for all products, the vertical average shows an increase in *FPR* toward the south pole, with PM-L2 showing the steepest increase.

3.3. Hemispheric and Seasonal Contrast

To assess the north-south contrast, we locate the region containing north-south *FPR* differences larger than +0.2, which we call the "contrast" region. Specifically, we compare the average position of the contrast region in the temperature-latitude space for the different products. For lower temperatures, the fraction of liquid clouds will also be lower and, therefore, the north-south contrast of *FPR* tends to decrease, as fewer clouds can glaciate. To assess the magnitude of the contrast despite this tendency, we normalize the hemispheric contrast by the supercooled liquid frequency (*SCF*) in the southern hemisphere:

$$\Delta FPR \, / \, SCF = \frac{FPR_{dusty} - \mathrm{FPR}_{clean}}{1 - \mathrm{FPR}_{clean}}, \tag{2}$$

where *dusty* corresponds to the northern hemisphere (or spring season) and *clean* to the southern hemisphere (or fall season). Thus, the normalized contrast represents the fraction of liquid clouds in the southern hemisphere that would glaciate in the northern hemisphere environment. Additionally, to compare the cloud-phase with the dust-aerosol contrast, we locate the region for which the dust concentration in the northern hemisphere is on average >50 times higher than in the southern hemisphere. Moreover, we note that already above 10°N the dust concentration is at least 10 times higher than in the southern hemisphere (not shown).

Figure 4 shows the location of the hemispheric and seasonal contrast of cloud-phase for the different products and the GDP2 ensemble. For all products, the contrast region is mostly located below −20 °C (Figure 4a). This result partly disagrees with other studies based on CALIOP and on the CPR, which have located the highest north-south contrast between −10 and −15 °C (Tan et al., 2014), and between −15 and −20 °C (Zhang et al., 2018). Nevertheless, the radar reflectivity used in Zhang et al. (2018) is meant to detect ice production (size and number) and is not a direct proxy for cloud top phase. On the other hand, the cloud-phase retrievals in Tan et al. (2014) use a different methodology (Choi et al., 2010) than for the GOCCP product (Cesana & Chepfer, 2013). The magnitude of the north-south contrast is also higher than previous estimates, where the contrast was reported to be about +0.05 *FPR* between −20 and −30 °C (Tan et al., 2014, for a more accurate comparison, please refer to the nonnormalized contrast in the supporting information). For the DARDAR and PM-L2 products, the contrast at 60°N/S extends up to about −12 and −17 °C, respectively. This may be related to the dust-aerosol contrast, which is higher between 60 and 70°N/S, mainly because of the very low concentrations over the Southern Ocean. However, the most notable difference between the products is the meridional extent of the contrast region. Toward the pole, the contrast region extends up to at least 70°N/S for all products; but toward the equator, the contrast extends down to 15°N/S, 25°N/S, and 40°N/S for the GOCCP, DARDAR, and PM-L2 products, respectively.

The North-South contrast in *FPR* is attributed by several authors to the hemispheric difference in aerosol loading (Kanitz et al., 2011; Li et al., 2017; Tan et al., 2014; Villanueva et al., 2020; Zhang et al., 2018). More specifically, it is attributed to the higher concentration of INP-active mineral dust aerosol in the northern hemisphere, mostly from the Sahara and Gobi deserts. However, the dust aerosol concentration in the northern hemisphere varies seasonally, with a peak during spring (Cowie et al., 2014; Zender & Kwon, 2005). For
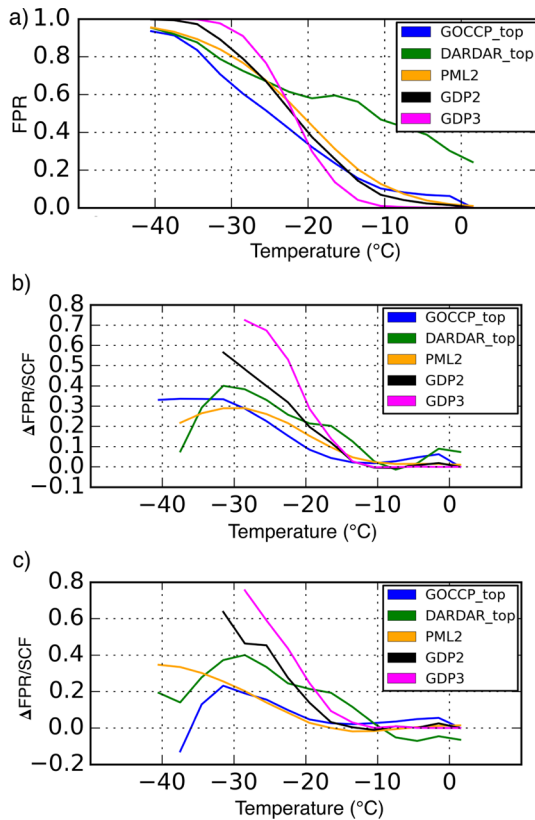
Figure 5. (a) Average frequency of ice cloud tops (*FPR*) at the midlatitudes 30–60°N/S. (b) Average north-south *FPR* difference at cloud top normalized by the supercooled liquid frequency (*SCF*) in the southern hemisphere. (c) Average seasonal *FPR* difference (MAM − SON) at cloud top at 30–60°N normalized by the *SCF* during SON. Only values for which the reference *SCF* is higher than 0.05 are shown. *FPR*, frequency phase ratio; MAM, March-April-May; SON, September-October-November.

this reason, we also analyzed the average *FPR* differences between the months of March-April-May (MAM) and September-October-November (SON). We defined the contrast regions where the MAM-SON(SON-MAM) difference in *FPR* is higher than +0.1 in the northern(southern) hemisphere. For the northern(southern) hemisphere, we normalize the seasonal contrast by the fraction of liquid clouds in SON(MAM). Additionally, we locate the regions for which the dust loading is at least three times higher during spring compared to autumn. Similar to the hemispheric contrast, the seasonal cloud-phase contrast is mostly located below −20 °C for all products (Figure 4b), in agreement with previous reports (Tan et al., 2014). In the northern midlatitudes, for DARDAR the seasonal contrast extends up to about −12 °C, while for GOCCP it extends only up to −22 °C. On the other hand, the meridional location of the seasonal contrast is very similar between the products, extending mostly from 30°N to 80°N. These contrasts, especially for the GOCCP product, have a "bow-tie" form, which is possibly related to the seasonal contrast of dust aerosol. In the southern hemisphere, between −31 and −25 °C, the PM-L2 product and the GDP2 ensemble show a seasonal contrast near 40°S.

We can retrieve some interesting features from the location of the hemispheric and seasonal contrast of cloud top phase. First, the GDP2 ensemble agrees best with the DARDAR product on the location of the hemispheric contrast, and with the PM-L2 product on the location of the seasonal contrast. Second, the "overlap" zone, where all three products show a hemispheric or seasonal contrast, lays mostly between −35 and −25 °C and between 40 and 70°N. At this temperature, most types of mineral dust act as efficient INP (Boose et al., 2016; Broadley et al., 2012; Murray et al., 2011). The overlap zone also coincides with the region where the contrast reaches a maximum for the GDP2 ensemble (see supporting information). Therefore, this high-contrast region offers a good target for future campaigns looking to study the north-south contrast in cloud glaciation.

3.4. Quantification and Attribution

We can use the GDP2 ensemble to identify the temperature range where individual cloud-phase products may be biased. In Section 3.2, it was shown that in the midlatitudes the DARDAR product overestimates the *FPR* (by +0.16) relative to the GDP2 ensemble, while the GOCCP product underestimates the *FPR* (by −0.05). Figure 5 shows the frequency of ice cloud tops, as well as the magnitude of the hemispheric and seasonal contrast of cloud-phase in the midlatitudes. In Figure 5a, we can see that the overestimation of the DARDAR product occurs mainly for temperatures above −25 °C, while for the GOCCP product the underestimation occurs mostly for temperatures below −15 °C.

By using only retrievals where all products agree on cloud-phase, we find that the cloud-phase transition occurs within a narrower temperature range. We recall that in the GDP2 ensemble, the cloud-phase is defined as long as all three individual products are available, even if they disagree. Alternatively, one can select only volume-gridboxes where all three products agree, which we call GDP3. As mentioned above, all three products agree on average only 60% of the time. For both GDP2 and GDP3, at −22 °C half of the cloud tops are classified as ice (Figure 5a). In the GDP3 ensemble, the cloud top phase transition is steeper and occurs only between −35 and −10 °C, while for GDP2 it occurs between −38 and 0 °C. The difference between the GDP2 and GDP3 ensembles can also be used to identify the clouds for which the products disagree upon. As can be seen from the difference in ice frequency between GDP2 and GDP3 (Figure 5a), these are mostly liquid clouds below −22 °C and ice clouds above −22 °C (as classified in the GDP3 ensemble), especially at −28 and −16 °C, respectively. These clouds may relate to some of the scenarios discussed in Section 2.1.

Table 1

The Sample Size n and Frequency Phase Ratio (FPR) of the Individual Cloud Products and the GDP Ensembles for Two Different Grid Choices

Grid lat × lon	n 2° × 2°	2° × 30°	FPR 2° × 2°	2° × 30°	Detrended (2008–2009)
GOCCP	83,097	64,640	0.45 ± 0.12	0.41 ± 0.13	0.52 ± 0.03
DARDAR	77,774	58,289	0.62 ± 0.05	0.61 ± 0.05	0.63 ± 0.02
PM-L2	662,690	157,020	0.60 ± 0.04	0.56 ± 0.04	0.63 ± 0.05
GDP-2	1,070	15,632	0.66 ± 0.16	0.52 ± 0.08	0.64 ± 0.05
GDP-3	262	4,027	0.75 ± 0.24	0.55 ± 0.14	0.74 ± 0.09

Note: The dataset includes the samples within the 30–60°N latitude band, at −22 °C. The estimated error corresponds to the monthly standard deviation during 2007–2010. For the de-trended dataset, the error corresponds to the standard deviation between the 12 monthly differences between 2008 and 2009.

The hemispheric and seasonal contrast in cloud-phase tends to increase at lower temperatures. In the midlatitudes, for temperatures higher than −10 °C, the hemispheric and seasonal contrasts in cloud-phase is close to zero for all products (Figures 5b and 5c). From −10 to −30 °C, both the hemispheric and seasonal contrast increases for all individual cloud products. Moreover, for the GDP2 and GDP3 the increase is higher than for the individual products. For temperatures below than −30 °C, the contrasts tend to decrease for the individual products. This decrease in the seasonal and hemispheric contrast for temperatures below −30 °C may be explained by the depletion of INP at higher altitudes.

The increase of cloud-phase contrast at lower temperatures coincides with the increasing effectivity of dust INP at lower temperatures. From −15 to −25 °C, both the seasonal and hemispheric contrast increase for all products by at least +0.15 (Figures 5b and 5c). This increment is even higher for the GDP2 (hemispheric: +0.33; seasonal: +0.41) and GDP3 ensemble (hemispheric: +0.59; seasonal: +0.56). This increase of the contrast for lower temperatures suggests that it may be driven by INP efficiency, which increases exponentially for decreasing temperature. In fact, as previously mentioned, dust INP generally starts to activate within this temperature range (Boose et al., 2016; Kanji et al., 2017; Niemand et al., 2012), and dust loading is higher in the northern-hemispheric spring (Cowie et al., 2014).

In other types of aerosol-cloud-interactions, such as the effect of cloud condensation nuclei on warm clouds, meteorological factors have been shown to dominate over the effect of aerosols (Gryspeerdt et al., 2016). In fact, meteorological factors such as wind speed and thermal stability may vary between hemispheres due to land-ocean distribution and affect the cloud ice frequency (Li et al., 2017). However, we also observe a cloud-phase contrast between spring and fall in the northern hemisphere, which is unlikely to be explained by the seasonal variability of such meteorological factors.

3.5. Uncertainty

For the individual products, the uncertainty associated with the hemispheric cloud-phase contrast arise mainly from retrieval issues in the GOCCP product and from the seasonal variability in PM-L2. Table 1 summarizes the uncertainty associated with each product. For 2° × 30°, the uncertainty in *FPR* is higher for GOCCP (±0.13; sample size $n = 64,640$) than for DARDAR (±0.05; $n = 58,289$). This higher uncertainty in GOCCP appears to be associated with a lower *FPR* from CALIOP during 2007, before the off-nadir angle was adjusted to decrease the specular reflection from ice crystals, which resulted in a bias in the detection of cloud-phase (Avery et al., 2020, see also supporting information). In addition, the uncertainty for PM-L2 (±0.04; $n = 662,690$) is similar to DARDAR despite a much higher sample size. This suggests that the error introduced from the monthly aggregation of FPR_{daily} (binary distributed; see Equation 1) cannot alone explain the differences in the spread of *FPR* for the different products. Table 2 summarizes the uncertainty associated with the hemispheric contrast in cloud-phase. The uncertainty in $\Delta FPR/SCF$ increases relative to *FPR*, partially due to the accumulation of error from both hemispheres. Particularly, for PM-L2, the standard deviation of $\Delta FPR/SCF$ is almost three times higher compared to *FPR*. We attribute this high uncertainty to the higher summer-winter variability of *FPR* in the PM-L2 product at 30–60°S (see supporting information), which leads to very low or negative hemispheric contrasts during boreal summer. For GOCCP, the change in the off-nadir angle of CALIOP during 2007 leads to an increase in *FPR* (see supporting information), which increases the standard deviation of *FPR*. However, for $\Delta FPR/SCF$ this anomaly during 2007 cancels out, and thus the increase in uncertainty is compensated by a lower interannual variability.

Table 2

As Table 1, but for ΔFPR/SCF, the Normalized Hemispheric Contrast (30–60° N/S)

Grid lat × lon	ΔFPR/SCF 2° × 2°	2° × 30°	Detrended (2008–2009)
GOCCP	0.16 ± 0.11	0.15 ± 0.13	0.22 ± 0.06
DARDAR	0.23 ± 0.08	0.25 ± 0.10	0.27 ± 0.07
PM-L2	0.20 ± 0.19	0.21 ± 0.21	0.20 ± 0.16
GDP-2	0.43 ± 0.36	0.31 ± 0.11	0.36 ± 0.12
GDP-3	0.79 ± 0.40	0.52 ± 0.17	0.58 ± 0.16

For the GDP ensembles, low sample sizes seem to result in a high uncertainty in the cloud-phase contrast. For the GDP2 ensembles (2° × 30° grid), the uncertainty associated with *FPR* and Δ*FPR*/*SCF* is inside the range observed for the individual products. However, the uncertainty associated with GDP3 is higher than for GDP2, probably due to a lower sample size (see again Equation 1). Similarly, the uncertainty for the GDP ensembles increases for finer grids, because the lower horizontal overlap between products in such grids results in a lower sample size. Due to this lower sample size, the uncertainty in *FPR* is about twice as high for the 2° × 2° grid compared to the 2° × 30° grid for both GDP2 and GDP3. For the normalized hemispheric contrast Δ*FPR*/*SCF*, the uncertainty is about three times as high for 2° × 2° compared to 2° × 30°. In summary, the GDP2 ensemble within a 2° × 30° grid produces the most accurate estimation of the hemispheric contrasts (±0.11).

The variability from the seasonal cycle affects the uncertainty in *FPR*, but not the uncertainty in Δ*FPR*/*SCF* from the GDP ensembles. To estimate the uncertainty associated with the detrended data set, we use the difference between each month of the year during 2008–2009. This excludes the seasonal variability and errors associated with the GOCCP product during 2007, as well as missing data from PM-L2 during 2010 (see supporting information). Therefore, the variability of the detrended data set can better represent the uncertainty associated with each product. For all individual products, the detrended data set has a lower uncertainty in *FPR* and Δ*FPR*/*SCF*. For PM-L2, the uncertainty of the detrended *FPR* and Δ*FPR*/*SCF* is at about twice as high compared to GOCCP and DARDAR. For the GDP2 and GDP3 ensembles, only the uncertainty in *FPR* decreases after detrending, while the uncertainty in Δ*FPR*/*SCF* does not change significantly. This suggests that for GDP2 and GDP3 the uncertainty in the hemispheric contrast is less affected by the seasonal variability and trends in the individual products.

4. Conclusions

Throughout the analysis, we used an ensemble of the GOCCP, DARDAR, and PM-L2 cloud top phase products as a reference to assess the confidence on the individual products. We attribute the differences between the *FPR* from the individual products to retrieval biases associated with each instrument. Such biases are related to the retrieval methods and the wavelength used, but also to cloud optical properties like particle size and optical depth.

We have shown that the GDP ensembles and the individual products mostly agree on the existence and location of the hemispheric and seasonal contrast in cloud top phase. These contrasts are centered near −30 °C and between 50 and 60°N. At −30 °C, using the GDP ensemble we find that, on average, half of the liquid cloud tops found in the southern midlatitudes glaciate in the northern midlatitudes. We find similar results for the seasonal contrast (spring relative to fall), though only in the northern hemisphere. In addition, the magnitude of the cloud-phase contrasts seems to be underestimated by the individual products. The location of the hemispheric and seasonal contrasts in cloud top phase is consistent with the contrasts in dust aerosol loading, which provides additional evidence of the global role of aerosol in controlling the variability of cloud-phase. By constraining the spatiotemporal variability of cloud-phase, we expect to improve the general understanding of the atmospheric differences between hemispheres. The new metric for quantifying the contrasts may help to elucidate the differences in cloud-phase and the radiative balance between hemispheres, as well as their relationship with aerosols and cloud glaciation. By locating the north-south and seasonal contrast of cloud top phase, we also provide a potential target for future in-situ campaigns looking to clarify the processes behind cloud glaciation.

In future studies, the hemispheric and seasonal contrast in cloud-phase may be used to constrain cloud glaciation, heterogeneous freezing rates, and the impact of dust INP in global climate models. Additionally, this new benchmark can be used to evaluate different climate models and different parameterizations of heterogeneous freezing from a large-scale perspective.

Data Availability Statement

The data set containing the GDP ensemble can be found at: https://catalogue.ceda.ac.uk/uuid/f742c505c935467ebb4cf89a611a4436.

References

Avery, M. A., Ryan, R. A., Getzewich, B. J., Vaughan, M. A., Winker, D. M., Hu, Y., & Verhappen, C. A. (2020). CALIOP v4 cloud thermodynamic phase assignment and the impact of near-nadir viewing angles. *Atmospheric Measurement Techniques*, *13*(8), 4539–4563. https://doi.org/10.5194/amt-13-4539-2020

Bodas-Salcedo, A., Williams, K. D., Ringer, M. A., Beau, I., Cole, J. N. S., Dufresne, J.-L., & Yokohata, T. (2014). Origins of the solar radiation biases over the Southern Ocean in CFMIP2 models. *Journal of Climate*, *27*(1), 41–56. https://doi.org/10.1175/JCLI-D-13-00169.1

Boose, Y., Welti, A., Atkinson, J., Ramelli, F., Danielczok, A., Bingemer, H. G., & Lohmann, U. (2016). Heterogeneous ice nucleation on dust particles sourced from nine deserts worldwide—Part 1: Immersion freezing. *Atmospheric Chemistry and Physics*, *16*(23), 15075–15095. https://doi.org/10.5194/acp-16-15075-2016

Broadley, S. L., Murray, B. J., Herbert, R. J., Atkinson, J. D., Dobbie, S., Malkin, T. L., & Neve, L. (2012). Immersion mode heterogeneous ice nucleation by an illite rich powder representative of atmospheric mineral dust. *Atmospheric Chemistry and Physics*, *12*(1), 287–307. https://doi.org/10.5194/acp-12-287-2012

Bruno, O., Hoose, C., Storelvmo, T., Coopman, Q., & Stengel, M. (2021). Exploring the cloud top phase partitioning in different cloud types using active and passive satellite sensors. *Geophysical Research Letters*, *48*, e2020GL089863. https://doi.org/10.1029/2020GL089863

Ceccaldi, M., Delanoë, J., Hogan, R. J., Pounder, N. L., Protat, A., & Pelon, J. (2013). From CloudSat-CALIPSO to EarthCare: Evolution of the DARDAR cloud classification and its comparison to airborne radar-lidar observations. *Journal of Geophysical Research: Atmospheres*, *118*, 7962–7981. https://doi.org/10.1002/jgrd.50579

Cesana, G., & Chepfer, H. (2013). Evaluation of the cloud thermodynamic phase in a climate model using CALIPSO-GOCCP. *Journal of Geophysical Research: Atmospheres*, *118*, 7922–7937. https://doi.org/10.1002/jgrd.50376

Choi, Y. S., Lindzen, R. S., Ho, C. H., & Kim, J. (2010). Space observations of cold-cloud phase change. *Proceedings of the National Academy of Sciences of the United States of America*, *107*(25), 11211–11216. https://doi.org/10.1073/pnas.1006241107

Coopman, Q., Riedi, J., Zeng, S., & Garrett, T. J. (2020). Space-based analysis of the cloud thermodynamic phase transition for varying microphysical and meteorological regimes. *Geophysical Research Letters*, *47*, e2020GL087122. https://doi.org/10.1029/2020GL087122

Cowie, S. M., Knippertz, P., & Marsham, J. H. (2014). A climatology of dust emission events from Northern Africa using long-term surface observations. *Atmospheric Chemistry and Physics*, *14*(16), 8579–8597. https://doi.org/10.5194/acp-14-8579-2014

Delanoë, J., & Hogan, R. J. (2010). Combined CloudSat-CALIPSO-MODIS retrievals of the properties of ice clouds. *Journal of Geophysical Research*, *115*, D00H29. https://doi.org/10.1029/2009JD012346

Ewald, F., Groß, S., Wirth, M., Delanoë, J., Fox, S., & Mayer, B. (2021). Why we need radar, lidar, and solar radiance observations to constrain ice cloud microphysics. *Atmospheric Measurement Techniques Discussion*, in review. https://doi.org/10.5194/amt-2020-448

Gryspeerdt, E., Quaas, J., & Bellouin, N. (2016). Constraining the aerosol influence on cloud fraction. *Journal of Geophysical Research: Atmospheres*, *121*, 3566–3583. https://doi.org/10.1002/2015JD023744

Hawcroft, M., Haywood, J. M., Collins, M., Jones, A., Jones, A. C., & Stephens, G. (2017). Southern Ocean albedo, inter-hemispheric energy transports and the double ITCZ: Global impacts of biases in a coupled model. *Climate Dynamics*, *48*(7–8), 2279–2295. https://doi.org/10.1007/s00382-016-3205-5

Hu, Y., Winker, D., Vaughan, M., Lin, B., Omar, A., Trepte, C., & Kuehn, R. (2009). CALIPSO/CALIOP cloud phase discrimination algorithm. *Journal of Atmospheric and Oceanic Technology*, *26*(11), 2293–2309. https://doi.org/10.1175/2009JTECHA1280.1

Huang, L., Jiang, J. H., Wang, Z., Su, H., Deng, M., & Massie, S. (2015). Climatology of cloud water content associated with different cloud types observed by A-Train satellites. *Journal of Geophysical Research: Atmospheres*, *120*, 4196–4212. https://doi.org/10.1002/2014JD022779

Huang, Y., Siems, S. T., Manton, M. J., Protat, A., & Delanoë, J. (2012). A study on the low-altitude clouds over the Southern Ocean using the DARDAR-MASK. *Journal of Geophysical Research*, *117*, D18204. https://doi.org/10.1029/2012JD017800

Inness, A., Ades, M., Agustí-Panareda, A., Barr, J., Benedictow, A., Blechschmidt, A. M., & Suttie, M. (2019). The CAMS reanalysis of atmospheric composition. *Atmospheric Chemistry and Physics*, *19*(6), 3515–3556. https://doi.org/10.5194/acp-19-3515-2019

Kanitz, T., Seifert, P., Ansmann, A., Engelmann, R., Althausen, D., Casiccia, C., & Rohwer, E. G. (2011). Contrasting the impact of aerosols at northern and southern midlatitudes on heterogeneous ice formation. *Geophysical Research Letters*, *38*, L17802. https://doi.org/10.1029/2011GL048532

Kanji, Z. A., Ladino, L. A., Wex, H., Boose, Y., Burkert-Kohn, M., Cziczo, D. J., & Krämer, M. (2017). Overview of ice nucleating particles. *Meteorological Monographs*, *58*, 1.1–1.33. https://doi.org/10.1175/amsmonographs-d-16-0006.1

Kawamoto, K., Yamauchi, A., Suzuki, K., Okamoto, H., & Li, J. (2020). Effect of dust load on the cloud top ice-water partitioning over northern middle to high latitudes with CALIPSO products. *Geophysical Research Letters*, *47*, e2020GL088030. https://doi.org/10.1029/2020GL088030

Li, J., Lv, Q., Zhang, M., Wang, T., Kawamoto, K., Chen, S., & Zhang, B. (2017). Effects of atmospheric dynamics and aerosols on the fraction of supercooled water clouds. *Atmospheric Chemistry and Physics*, *17*(3), 1847–1863. https://doi.org/10.5194/acp-17-1847-2017

Luo, T., Wang, Z., Zhang, D., Liu, X., Wang, Y., & Yuan, R. (2015). Global dust distribution from improved thin dust layer detection using A-Train satellite lidar observations. *Geophysical Research Letters*, *42*, 620–628. https://doi.org/10.1002/2014GL062111

Matus, A. V., & L'Ecuyer, T. S. (2017). The role of cloud phase in Earth's radiation budget. *Journal of Geophysical Research: Atmospheres*, *122*, 2559–2578. https://doi.org/10.1002/2016JD025951

McCoy, D. T., Tan, I., Hartmann, D. L., Zelinka, M. D., & Storelvmo, T. (2016). On the relationships among cloud cover, mixed-phase partitioning, and planetary albedo in GCMs. *Journal of Advances in Modeling Earth Systems*, *8*, 650–668. https://doi.org/10.1002/2015MS000589

Mioche, G., Jourdan, O., Ceccaldi, M., & Delanoë, J. (2014). Variability of the mixed phase in the Arctic with a focus on the Svalbard region: A study based on spaceborne active remote sensing. *Atmospheric Chemistry and Physics Discussions*, *14*(16), 23453–23497. https://doi.org/10.5194/acpd-14-23453-2014

Morrison, A. E., Siems, S. T., & Manton, M. J. (2011). A three-year climatology of cloud-top phase over the Southern Ocean and North Pacific. *Journal of Climate*, *24*(9), 2405–2418. https://doi.org/10.1175/2010JCLI3842.1

Murray, B. J., Broadley, S. L., Wilson, T. W., Atkinson, J. D., & Wills, R. H. (2011). Heterogeneous freezing of water droplets containing kaolinite particles. *Atmospheric Chemistry and Physics*, *11*(9), 4191–4207. https://doi.org/10.5194/acp-11-4191-2011

Niemand, M., Möhler, O., Vogel, B., Vogel, H., Hoose, C., Connolly, P., & Leisner, T. (2012). A particle-surface-area-based parameterization of immersion freezing on desert dust particles. *Journal of the Atmospheric Sciences*, *69*(10), 3077–3092. https://doi.org/10.1175/JAS-D-11-0249.1

Pavolonis, M. J., Heidinger, A. K., & Uttal, T. (2005). Daytime global cloud typing from AVHRR and VIIRS: Algorithm description, validation, and comparisons. *Journal of Applied Meteorology*, *44*(6), 804–826. https://doi.org/10.1175/JAM2236.1

Riedi, J., Marchant, B., Platnick, S., Baum, B. A., Thieuleux, F., Oudard, C., & Dubuisson, P. (2010). Cloud thermodynamic phase inferred from merged POLDER and MODIS data. *Atmospheric Chemistry and Physics*, *10*, 11851–11865. https://doi.org/10.5194/acp-10-11851-2010

Seifert, P., Ansmann, A., Mattis, I., Wandinger, U., Tesche, M., Engelmann, R., & Haustein, K. (2010). Saharan dust and heterogeneous ice formation: Eleven years of cloud observations at a central European EARLINET site. *Journal of Geophysical Research*, *115*, D20201. https://doi.org/10.1029/2009JD013222

Stengel, M., Stapelberg, S., Sus, O., Finkensieper, S., Würzler, B., Philipp, D., & McGarragh, G. (2020). Cloud_cci advanced very high resolution radiometer post meridiem (AVHRR-PM) dataset version 3: 35-year climatology of global cloud and radiation properties. *Earth System Science Data*, *12*(1), 41–60. https://doi.org/10.5194/essd-12-41-2020

Sullivan, S. C., Lee, D., Oreopoulos, L., & Nenesa, A. (2016). Role of updraft velocity in temporal variability of global cloud hydrometeor number. *Proceedings of the National Academy of Sciences of the United States of America*, *113*(21), 5791–5796. https://doi.org/10.1073/pnas.1514039113

Tan, I., Storelvmo, T., & Choi, Y. S. (2014). Spaceborne lidar observations of the ice-nucleating potential of dust, polluted dust, and smoke aerosols in mixed-phase clouds. *Journal of Geophysical Research: Atmospheres*, *119*, 6653–6665. https://doi.org/10.1002/2013JD021333

Tan, I., Storelvmo, T., & Zelinka, M. D. (2016). Observational constraints on mixed-phase clouds imply higher climate sensitivity. *Science*, *352*(6282), 224–227. https://doi.org/10.1126/science.aad5300

Trenberth, K. E., & Fasullo, J. T. (2010). Simulation of present-day and twenty-first-century energy budgets of the Southern Oceans. *Journal of Climate*, *23*(2), 440–454. https://doi.org/10.1175/2009JCLI3152.1

Vergara-Temprado, J., Miltenberger, A. K., Furtado, K., Grosvenor, D. P., Shipway, B. J., Hill, A. A., & Carslaw, K. S. (2018). Strong control of Southern Ocean cloud reflectivity by ice-nucleating particles. *Proceedings of the National Academy of Sciences of the United States of America*, *115*(11), 2687–2692. https://doi.org/10.1073/pnas.1721627115

Vergara-Temprado, J., Murray, B. J., Wilson, T. W., O'Sullivan, D., Browse, J., Pringle, K. J., & Carslaw, K. S. (2017). Contribution of feldspar and marine organic aerosols to global ice nucleating particle concentrations. *Atmospheric Chemistry and Physics*, *17*(5), 3637–3658. https://doi.org/10.5194/acp-17-3637-2017

Villanueva, D., Heinold, B., Seifert, P., Deneke, H., Radenz, M., & Tegen, I. (2020). The day-to-day co-variability between mineral dust and cloud glaciation: A proxy for heterogeneous freezing. *Atmospheric Chemistry and Physics*, *20*(4), 2177–2199. https://doi.org/10.5194/acp-20-2177-2020

Wu, Y., Cordero, L., Gross, B., Moshary, F., & Ahmed, S. (2014). Assessment of CALIPSO attenuated backscatter and aerosol retrievals with a combined ground-based multi-wavelength lidar and sunphotometer measurement. *Atmospheric Environment*, *84*, 44–53. https://doi.org/10.1016/j.atmosenv.2013.11.016

Zelinka, M. D., Myers, T. A., McCoy, D. T., Po-Chedley, S., Caldwell, P. M., Ceppi, P., & Taylor, K. E. (2020). Causes of higher climate sensitivity in CMIP6 models. *Geophysical Research Letters*, *47*, e2019GL085782. https://doi.org/10.1029/2019GL085782

Zender, C. S., & Kwon, E. Y. (2005). Regional contrasts in dust emission responses to climate. *Journal of Geophysical Research*, *110*, D13201. https://doi.org/10.1029/2004JD005501

Zhang, D., Wang, Z., Heymsfield, A., Fan, J., Liu, D., & Zhao, M. (2012). Quantifying the impact of dust on heterogeneous ice generation in midlevel supercooled stratiform clouds. *Geophysical Research Letters*, *39*, L18805. https://doi.org/10.1029/2012GL052831

Zhang, D., Wang, Z., Kollias, P., Vogelmann, A. M., Yang, K., & Luo, T. (2018). Ice particle production in mid-level stratiform mixed-phase clouds observed with collocated A-Train measurements. *Atmospheric Chemistry and Physics*, *18*(6), 4317–4327. https://doi.org/10.5194/acp-18-4317-2018